Word Count: 5854

Revision 1

Validation of clinopyroxene–garnet magnesium isotope geothermometer to constrain the peak metamorphic temperature in ultrahigh-temperature ultramafic-mafic granulites

Long-Long Gou[1], Ming-Guo Zhai[1,2*], Cheng-Li Zhang[1], P.M. George[1], Kang-Jun Huang[1], Xiao-Fei Xu[1], Jun-Sheng Lu[1], Yan Zhao[1], Wen-Hao Ao[1], Yu-Hua Hu[1], Feng Zhou[1]

[1]*State Key Laboratory of Continental Dynamics, Department of Geology, Northwest University, Xi'an 710069, China*

[2] *State Key Laboratory of Lithospheric Evolution, Institute of Geology and Geophysics, Chinese Academy of Sciences, Beijing 100029, China*

(*corresponding author: mgzhai@mail.iggcas.ac.cn)

ABSTRACT

Conventional Fe–Mg exchange geothermometers generally are not effective means to measure the peak metamorphic temperatures of granulites, because of Fe-Mg diffusion during the re-equilibration during the exhumation and cooling. Therefore, it is essential to find alternative geothermometers. In this study, we investigated the magnitude of Mg isotope fractionation between the co-exsiting clinopyroxene and garnet in garnet pyroxenites and high-pressure mafic granulites from southern India. The clinopyroxene and garnet from the garnet pyroxenites have $\delta^{26}Mg$ values of −0.04‰ to −0.07‰, and −0.65‰ to −0.64 ‰, respectively, with $\Delta^{26}Mg_{clinopyroxene–garnet} = \delta^{26}Mg_{clinopyroxene} - \delta^{26}Mg_{garnet}$ = 0.62‰ and 0.57‰. The $\delta^{26}Mg$ values of the coexisting clinopyroxene and garnet in the high-pressure mafic granulites, are 0.03‰ to 0.07‰, and −0.54‰ to −0.55‰, respectively, with $\Delta^{26}Mg_{clinopyroxene–garnet}$ = 0.57‰ and 0.62‰. The inter-mineral Mg isotope fractionations between the clinopyroxene and garnet of the garnet pyroxenites are similar to those of the high-pressure mafic granulites, and more or less fall within the equilibrium fractionation lines at peak metamorphic temperatures. The measured peak temperatures for all four samples indicate equilibrium Mg isotope fractionations between the clinopyroxene and garnet. The clinopyroxene–garnet Mg isotope geothermometer of Li et al. (2016) yields temperatures of 994 ± 60 °C and 1048 ± 89 °C for the garnet pyroxenites, and 1048 ± 89 °C and 994 ± 65 °C for the high-pressure mafic granulites, which are slightly lower than those at both 10 kbar and 12 kbar from the clinopyroxene–

garnet Mg isotope thermometer of Huang et al. (2013). Compared with the peak metamorphic conditions from phase equilibrium modelling, the clinopyroxene–garnet Mg isotope thermometry yielded temperatures corresponding to the peak metamorphic conditions of the garnet pyroxenites and the high-pressure mafic granulites, whereas the conventional clinopyroxene–garnet Fe–Mg exchange thermometry yielded lower temperatures corresponding to the retrograde metamorphism. These results underscore the inter-mineral Fe–Mg exchange between clinopyroxene and garnet during the retrograde cooling of the ultrahigh-temperature (>900 °C); but however did not disturb their Mg isotope fractionation equilibrium attained during the ultrahigh-temperature metamorphic condition. Therefore, we conclude that clinopyroxene–garnet Mg isotope thermometry, together with phase equilibrium modelling, is a valid tool to constrain the peak metamorphic temperature conditions even for ultramafic-mafic granulites that have undergone ultrahigh-temperature metamorphism.

Keywords: Clinopyroxene–garnet Mg isotope geothermometer, Mg isotope fractionation, Garnet pyroxenites, High-pressure mafic granulites

INTRODUCTION

It's well known that granulites provide a window to understand the accretion and eventual stabilization of new crust and hence continental growth (Bohlen and Mezger, 1989; Harley 1989; Sawyer et al. 2011; Cipar et al. 2020), but conventional Fe–Mg exchange geothermometers generally underestimate the peak metamorphic temperatures

of granulites (Frost and Chacko 1989; Harley 1989, 1998; Fitzsimons and Harley 1994; Pattison et al. 2003; Usuki et al. 2017), due to the fast Fe–Mg diffusion during retrograde cooling obliterated initial mineral compositions. Therefore, it is important to look for alternative geo-thermometers to estimate the peak metamorphic temperature, unaffected by the late re-equilibrium processes. Several attempts were made in this regard in the past decade, and the Mg isotope geothermometer may be a good candidate, as mentioned below. A large inter-mineral Mg isotope fractionation of $\Delta^{26}Mg_{clinopyroxene–garnet} = 1.14 \pm 0.04‰$ was found in a set of eclogites from Bixiling in the Dabie orogen, China (Li et al. 2011). The constant inter-mineral Mg isotope fractionation, together with homogeneous mineral chemistry and equilibrium oxygen isotopic partitioning between clinopyroxene and garnet, suggests an equilibrium Mg isotope fractionation (Li et al. 2011). Later analyses of coexisting clinopyroxene and garnet in cratonic eclogites (Wang et al. 2012, 2015) and orogenic eclogites (Wang et al. 2014a, b; Li et al. 2016) also found large equilibrium inter-mineral Mg isotope fractionation. This large equilibrium Mg isotope fractionation is controlled by different coordination numbers of Mg in these two minerals, with six in clinopyroxene and eight in garnet, as minerals with lower coordination number favoring heavier isotopes when thermodynamic equilibrium is achieved (Li et al. 2011, 2016; Wang et al. 2012, 2015; Huang et al. 2013; Young et al. 2015). As a result, equilibrium fractionation of Mg isotope between clinopyroxene and garnet could be used as a geothermometer, with high-precision and wide applications in igneous and metamorphic rocks where garnet co-exists with clinopyroxene (Huang et al. 2013; Li et al.

2016).

However, experiment results demonstrated large Mg isotope fractionation associated with diffusion of Mg along chemical and temperature gradients (Richter et al. 2008; Huang et al. 2009, 2010; Chopra et al. 2012). Further studies on natural samples demonstrated that there was Mg isotope fractionation related to chemical diffusion at both mineral and outcrop scales (Teng et al. 2011; Chopra et al. 2012; Sio et al. 2013; Oeser et al. 2015; Pogge Von Strandmann et al. 2015; Teng 2017). Therefore, it's worth to investigate whether the inter-mineral diffusion exchange of Fe–Mg during the retrograde metamorphism of granulites affect the equilibrium Mg isotope fractionation between clinopyroxene and garnet that achieved under peak metamorphic conditions. This not only can answer if the clinopyroxene–garnet Mg isotope geothermometer could be applied to constrain the peak temperature of clinopyroxene- and garnet-bearing granulites, but also help us to understand the Mg isotope fractionation during the granulite-facies metamorphism.

In this study, we carried out Mg isotopic analyses of clinopyroxenes and garnets from newly discovered garnet pyroxenites and high-pressure (HP) mafic granulites from the Namakkal Block of the Southern Granulite Terrane (SGT), India, and investigated the magnitude of Mg isotope fractionation between clinopyroxene and garnet in these ultramafic-mafic granulites. On the basis of results from phase equilibrium modelling,

mineral chemical analysis, conventional clinopyroxene–garnet Fe–Mg exchange geothermometry, and clinopyroxene–garnet Mg isotope geothermometry, we evaluate the feasibility of clinopyroxene–garnet Mg isotope geothermometer in these ultramafic-mafic granulites, and the effect of the retrograde cooling on equilibrium Mg isotope fractionation between clinopyroxene and garnet during the peak metamorphism.

GEOLOGICAL SETTING AND SAMPLE DESCRIPTION

The SGT, located at the southern margin of the Dharwar Craton, is composed of the Coorg, Nilgiri, Billigiri Rangan, Shevaroy, Madras, and Namakkal granulite Blocks (Figure 1). The Namakkal Block or the Kolli-massif (George and Sajeev, 2015) is composed of charnockite, HP mafic granulite, garnet pyroxenite, ultramafic rocks, anorthosite, gneiss, granite, migmatite, and minor layers of banded magnetite quartzite (Figure 2) (Anderson et al. 2012; Mohan et al. 2013; Glorie et al. 2014; George et al. 2019; Peng et al. 2019; He et al. 2020, 2021). Zircon and monazite U–Pb analyses on various metamorphic rocks have yielded metamorphic ages ranging from 2526 to 2442 Ma (Saitoh et al. 2011; Sato et al. 2011; Anderson et al. 2012; Mohan et al. 2013; Glorie et al. 2014; George et al. 2019; Peng et al. 2019; Talukdar et al. 2020). Phase equilibrium modelling yielded a *P–T* condition of 22 kbar at 980 °C for the garnet pyroxenite from the Jambumalai Hills in the Kolli-massif (Figure 2), and an isothermal decompression *P–T* path was obtained based on the presence of plagioclase corona around the garnet (George et al. 2019). The HP mafic granulites from the Mahadevi Layered complex

(MLC), record a simultaneous cooling and decompression *P–T* path, with peak metamorphism that occurred under HP granulite-facies condition of ~800 °C at 12–14 kbar, and retrograde metamorphism under *P–T* conditions of ~10–11 kbar, ~710 °C and ~6–8 kbar, >580–620 °C (Chowdhury and Chakraborty 2019).

Four representative ultramafic-mafic granulite samples were selected for this study on the basis of detailed petrology, which are garnet pyroxenite samples 18ID-39 and 18ID-41 (Figure 3a, b), and HP mafic granulite samples 18ID-46 and 18ID-50 (Figure 3c–f). The garnet pyroxenite samples 18ID-39 and 18ID-41 are mainly composed of garnet and clinopyroxene, plagioclase, ilmenite and hematite (Figures 3a, b and S1a, b), and accessory apatite (Figure S1a). Minor hornblende and quartz occur as tiny interstitial grains (Figure S1a, b), and are considered to have formed during the retrograde cooling. These garnet pyroxenite samples display granoblastic texture (Figure 3a, b), indicating high equilibrium temperature. Clinopyroxene develops extremely narrow orthopyroxene exsolution lamellae (Figure 4a, b), which is considered as a result of the retrograde cooling. Ilmenite and hematite are relatively abundant in the garnet pyroxenite and are present as interstitial grains (Figures 3a, b and S1a, b). Ilmenite commonly contains hematite exsolution lamellae (Figure S1a, b). As a result, the peak metamorphic phase assemblage of the garnet pyroxenites, is inferred to have been garnet–clinopyroxene–plagioclase–ilmenite–melt, and the final subsolidus mineral assemblage preserved in these samples comprises garnet–clinopyroxene–hornblende–plagioclase–ilmenite–

142 hematite–quartz.

143

144 The HP mafic granulite samples 18ID-46 and 18ID-50 mainly consist of garnet,
145 clinopyroxene, orthopyroxene, hornblende and plagioclase (Figure 3c–f), with minor
146 quartz, and accessory ilmenite, hematite and zircon (Figure S1c, d). They also display
147 granoblastic texture (Figure 3c–f). Plagioclase is more abundant than that in the garnet
148 pyroxenites (Figure 3a–f). Only minor quartz was observed, which occurs as narrow
149 films or tiny grains along the boundary between other minerals (Figure S1c, d).
150 Hornblende occurs as corona around clinopyroxene and orthopyroxene, or as interstitial
151 grains between garnet, clinopyroxene and orthopyroxene (Figure 3d, f). Thus, the quartz
152 and hornblende in the HP mafic granulites are inferred to have formed during the
153 retrograde metamorphism. It can be noted that sample 18ID-46 contains abundant
154 hornblende, whereas sample 18ID-50 contains only minor hornblende, which are due to
155 different degrees of retrograde metamorphism. Extremely narrow orthopyroxene
156 exsolution lamellae has also been observed in the clinopyroxene in the two HP mafic
157 granulite samples (Figure 4c, d), which might have formed as a result of retrograde
158 cooling. Hematite exsolution lamellae can be also observed in ilmenite (Figure S1d).
159 Hence, the peak metamorphic phase assemblage of the HP mafic granulites, is inferred to
160 have been garnet–clinopyroxene–orthopyroxene–plagioclase–ilmenite–melt, and the
161 subsolidus mineral assemblage preserved in these sample comprises garnet–
162 clinopyroxene–orthopyroxene–hornblende–plagioclase–ilmenite–hematite–quartz.

ANALYTICAL METHODS

Mineral compositional analysis

Mineral compositions were analyzed using the JEOL JXA-8230 electron microprobe (EMP) at the State Key Laboratory of Continental Dynamics (SKLCD), Northwest University, Xi'an. The operating conditions are 2 μm beam size, 15 kV acceleration voltage, and 10 nA beam current. Mineral formula was calculated from the EMP data, based on the stoichiometric charge balance, using the program AX (https://filedn.com/lU1GlyFhv3UuXg5E9dbnWFF/TJBHpages/ax.html), except for Fe^{3+} content in clinopyroxene (calculated by end-member method). Mineral compositions and the mole fractions of end-members for the garnet pyroxenite samples 18ID-39 and 18ID-41, and the HP mafic granulite samples 18ID-46 and 18ID-50 are given in Tables S1, S2, S3 and S4, respectively. As the clinopyroxene in both the garnet pyroxenites and HP mafic granulites displays exsolution lamellar of orthopyroxene, re-integrated pre-exsolution original compositions of clinopyroxene were calculated from the compositions of host and lamellar domains, and the mass proportions. The mass proportions were calculated using areal proportions (assumed to be equal to volume propositions) of host-lamellae estimated from back-scattered images (Figure 4), and densities of clinopyroxene (3.27 g/cm^3) and orthopyroxene (3.61 g/cm^3). The re-integrated compositions are listed in Table S5.

Tescan Integrated Mineral Analyzer (TIMA) at the SKLCD, Northwest University, Xi'an, was used to determine hornblende and quartz in the ultramafic-mafic granulites, with a beam current of 8.66 nA, beam energy of 25 kV, and working distance of 15 mm.

Pseudosection modelling

Phase equilibrium modelling was carried out on the garnet pyroxenite sample 18ID-39 and HP mafic granulite sample 18ID-50, to constrain the peak metamorphic *P–T* condition. The bulk chemical compositions (Table 1) were determined by wavelength-dispersive X-ray fluorescence (XRF) spectrometry at the SKLCD (Rigaku RIX 2100) on a fused bead, except for FeO versus Fe_2O_3 (total iron was determined as Fe_2O_3 by the XRF) and the H_2O content. The amount of FeO was determined by titration and then Fe_2O_3 was calculated by difference. The loss on ignition is negative as the Fe^{2+} was oxidized to Fe^{3+} during the heating. The modelled bulk-rock H_2O content in *P–T* pseudosection modelling was adjusted using T–X_{H2O} pseudosection, so that the final phase assemblage is stable just above the solidus, which is assumed to reflect the conditions where this assemblage would have been in equilibrium with the last remaining melt (Korhonen et al., 2013). Phase equilibrium calculation was performed using THERMOCALC version tc345 (Powell et al. 1998) with the internally consistent thermodynamic dataset ds62 (Holland and Powell 1998, 2011) and the activity–composition (a–x) models for the Na_2O–CaO–K_2O–FeO–MgO–Al_2O_3–SiO_2–H_2O–TiO_2–O_2 (NCKFMASHTO) system (White et al. 2014; Green et al. 2016).

Garnet–clinopyroxene Fe–Mg thermometry

The garnet–clinopyroxene Fe–Mg thermometer of Ravna (2000) was adopted to calculate the metamorphic temperatures for the garnet pyroxenites and HP mafic granulites. The compositions of garnet and clinopyroxene cores were used, as they record higher metamorphic temperatures than those of rims. The re-integrated pre-exsolution original compositions of clinopyroxene were also used to calculate metamorphic temperature, in order to determine whether the exsolution lamellar of orthopyroxene significantly affect the calculated temperature results. The calculated temperature results are presented in Table 2.

Mg isotopic analysis

Solution preparation was performed in an ultra-clean room at the SKLCD. The garnet and clinopyroxene separated from the crushed samples of the garnet pyroxenites and HP mafic granulites were ground to powder using agate mortar, and then an appropriate amount of powder was weighted to obtain ~25 μg Mg for chemical purification based on the MgO content. Weighted powders were placed in 15 mL Savillex Teflon beakers with a mixture of concentrated HF–HNO_3 (3 : 1). The beakers were heated overnight at a temperature of 120 °C on a hot plate, and then the solutions were evaporated to dryness. The dried samples were refluxed with concentrated HNO_3 to remove residual fluorides, and then were made to evaporate again. After the precipitation and centrifugation, the

dissolved rock solutions containing 25 μg Mg were passed through two columns containing AG50W-X12 cation exchange resins to eliminate matrix elements. The collected solutions were then evaporated at 80 °C, and the residues were dissolved in 2% HNO_3 for measurement.

Analysis of Mg isotope ratios was carried out on a Nu Plasma II MC-ICPMS (Nu Instruments, Wrexham, UK) at the SKLCD. The standard-sample-standard bracketing method was used to correct the instrumental mass bias during the analyses, and the standard solution was GSB-Mg (Bao et al. 2020). The Mg isotopic ratios were first normalized to the GSB-Mg standard by $\delta^{x}Mg_{Sample\text{-}Standard} = 10^{3} \times \{2 \times ({}^{x}Mg/{}^{24}Mg)_{Sample(i)}/[({}^{x}Mg/{}^{24}Mg)_{Standard(i)} + ({}^{x}Mg/{}^{24}Mg)_{Standard(i+1)}] - 1\}$ (Teng 2017), where x refers to mass 25 or 26. Then, the $\delta^{x}Mg_{Sample\text{-}Standard}$ was converted to $\delta^{x}Mg_{Sample\text{-}DSM3}$ using the following formula: $\delta^{x}Mg_{Sample\text{-}DSM3} = \delta^{x}Mg_{Sample\text{-}Standard} + \delta^{x}Mg_{Standard\text{-}DSM3} + 10^{-3} \times \delta^{x}Mg_{Sample\text{-}Standard} \times \delta^{x}Mg_{Standard\text{-}DSM3}$ (Galy et al. 2003). The $\delta^{26}Mg$ and $\delta^{25}Mg$ values of the GSB-Mg standard solution relative to DSM3 are −2.049‰ and −1.056‰, with uncertainty of 0.049‰ and 0.028‰, respectively (Bao et al. 2020). The USGS basalt standards BCR-2 and BHVO-2, and procedural blank were processed through column chemistry with samples to check the accuracy. The measured Mg isotopic compositions agree well with previously reported values (Table 3; Bizzarro et al. 2011; An et al. 2014; Teng et al. 2015; Bao et al. 2019). The detailed description of the methodology used in SKLCD can be found in Bao et al. (2019).

Clinopyroxene–garnet Mg isotope thermometry

The calibrations of clinopyroxene–garnet Mg isotope thermometers from both Li et al. (2016) and Huang et al. (2013) were applied to the garnet pyroxenites and the HP mafic granulites. The clinopyroxene–garnet Mg isotope thermometer of Li et al. (2016) was calibrated by natural samples, whereas that of Huang et al. (2013) was on the basis of first-principles calculation of equilibrium Mg isotope fractionations between garnet and clinopyroxene. The pressure effect was not considered in the clinopyroxene–garnet Mg isotope thermometer of Li et al. (2016), whereas the pressures of 10 and 12 kbar based on phase equilibrium modellings of the garnet pyroxenites and the HP mafic granulites were adopted, when the clinopyroxene–garnet Mg isotope thermometer of Huang et al. (2013) was applied, as Huang et al. (2013) has revealed substantial pressure effect on Mg isotope fractionation between garnet and clinopyroxene.

RESULTS

Mineral chemistry

Compositions of garnet, clinopyroxene and orthopyroxene exsolution lamellae were analyzed for both the garnet pyroxenites and HP mafic granulites. Garnet in the garnet-pyroxenite sample 18ID-39 is rich in almandine (X_{Alm} = 0.51–0.54), pyrope (X_{Prp} = 0.27–0.30) and grossular (X_{Grs} = 0.17–0.18), with low abundances of spessartine (X_{Sps} = ~0.01) (Table S1). Clinopyroxene in the sample 18ID-39 is diopside in composition,

with low Na of 0.04–0.05 cations per formula unit (cpfu) (Table S1), and their Mg# and Al are 0.68–0.73 and 0.18–0.25 cpfu, respectively (Table S1). Compositional profile displays that both garnet and clinopyroxene have no significant variation in Mg# from core to rim (Table S1; Figure 5a). Orthopyroxene exsolution lamellae has Mg# value of 0.54–0.55 (Table S1).

The compositions of garnet, clinopyroxene and orthopyroxene exsolution lamellae in the garnet pyroxenite sample 18ID-41 are similar to those of the sample 18ID-39 (Tables S1 and S2; Figure 5a, b). However, the garnet in the sample 18ID-41 has feeble compositional variation from core to rim, with increasing pyrope and Mg# but decreasing almandine close to the rim (Table S2; Figure 5b), due to subsolidus retrograde Fe–Mg exchange. In addition, clinopyroxene exhibits a weak increase in Mg# close to the rim (Table S2; Figure 5b). Orthopyroxene exsolution lamellae has Mg# ranging from 0.53 to 0.56 (Table S2).

Garnet in the HP mafic granulite sample 18ID-46 is almandine-, pyrope- and grossular-rich (X_{Alm} = 0.58–0.60; X_{Prp} = 0.20–0.22; X_{Grs} = 0.18–0.19), with low concentration of spessartine (X_{Sps} = ~0.01) (Table S3); and it displays a weak variation in composition from core to rim, with increasing almandine but decreasing pyrope and Mg# close to the rim (Table S3; Figure 5c), due to subsolidus retrograde Fe–Mg exchange. Clinopyroxene is diopside in composition, with Mg# value of 0.64–0.75, and exhibits

283 only weak compositional variation from core to rim, with increasing Mg# close to the rim
284 (Tables S3; Figure 5c). Orthopyroxene exsolution lamellae has uniform Mg# of 0.51–
285 0.52 (Table S3).
286
287 The compositions of garnet, clinopyroxene and orthopyroxene exsolution lamellae in the
288 HP mafic granulite sample 18ID-50 are similar to those of the sample 18ID-46 (Tables S3
289 and S4; Figure 5c, d). Garnet exhibits weak compositional zoning from core to rim, with
290 increasing almandine but decreasing pyrope and Mg# close to the rim (Table S4; Figure
291 5d). The zoning profile of clinopyroxene also shows only weak compositional variation
292 from core to rim, with increasing Mg# close to the rim (Tables S4; Figure 5d).

293 ***P–T* pseudosection**

294 **Garnet pyroxenite sample 18ID-39**

295 A T–X_{H2O} pseudosection was calculated at 10 kbar (Figure 6a), which is within the
296 pressure range for the final phase assemblage of grt–hbl–cpx–pl–ilm–qz–liq (Figure 6b).
297 The H_2O contents investigated on Figure 6a range from an anhydrous composition (X_{H2O}
298 = 0) to the H_2O content of 5.0 mol.% (X_{H2O} = 1) (Table 1). A X_{H2O} value of 0.45 (2.25
299 mol.% H_2O, Table 1; red bar on Figure 6a) was selected for subsequent P–T
300 pseudosection modelling of this bulk composition, which corresponds to the mid-point of
301 the solidus curve for the final phase assemblage (Figure 6a).
302

303 The calculated *P–T* pseudosection (Figure 6b), allows the mineral assemblages to be
304 evaluated over a range of *P–T* conditions. The peak phase assemblage grt–cpx–pl–ilm–liq
305 occurs between 1080 and 1130 °C and 8.7–10.7 kbar (Figure 6b). The garnet-out line
306 marks the upper temperature limit of this field (Figure 6b). The upper pressure and low
307 temperature limits are the plagioclase-out and hornblende-in assemblage field boundaries,
308 respectively (Figure 6b).

309 **HP mafic granulite sample 18ID-50**

310 A $T–X_{H2O}$ pseudosection for the HP mafic granulite sample 18ID-50 was also calculated
311 at 10 kbar (Figure 6c), which is consistent with the pressure range for the final phase
312 assemblage of grt–hbl–cpx–opx–pl–ilm–qz–liq (Figure 6d). A similar approach to that
313 described above for sample 18ID-39 was used to constrain appropriate H_2O content for
314 the *P–T* pseudosection (Figure 6c; Table 1). A X_{H2O} value of 0.06 (0.30 mol.% H_2O, Table
315 1; red bar on Figure 6c), corresponding to the mid-point of the solidus curve for the final
316 phase assemblage (Figure 6d), was selected for subsequent *P–T* pseudosection
317 calculation.
318
319 The peak phase assemblage of the HP mafic granulite is represented by the hexa-variant
320 field grt–cpx–opx–pl–ilm–melt in the calculated *P–T* pseudosection (Figure 6d), which
321 occurs between 910 °C and 1140 °C and 9.0–12.4 kbar (Figure 6d). The hornblende-in
322 assemblage field boundary marks the low temperature limit of this field and the

garnet-out assemblage field boundary marks the upper-temperature limit. The upper-pressure limit is the quartz-in assemblage field boundary. Calculated isopleths of X_{An} for plagioclase, and X_{Grs} for garnet, were contoured in the *P–T* pseudosection (Figure 6d). Using the X_{An} in plagioclase (0.44–0.48) and the mole fraction of grossular in garnet (0.18–0.19) (Table S4), the peak *P–T* condition was further constrained to be *T* = 1070–1110 ºC at *P* = 11.5–12.2 kbar (Figure 6d).

Metamorphic temperatures from the garnet–clinopyroxene Fe–Mg thermometry

The peak *P–T* conditions of the garnet pyroxenites and HP mafic granulites are constrained to be 1080–1130 °C at 8.7–10.7 kbar (Figure 6b) and 1070–1110 °C at 11.5–12.2 kbar (Figure 6d) from the phase-equilibrium modelling, respectively. Thus, the pressure should be set to 10 kbar, when the garnet–clinopyroxene Fe–Mg thermometry is applied to the garnet pyroxenites, and on the other hand, the pressure should be set to 12 kbar during application of the garnet–clinopyroxene Fe–Mg thermometry to the HP mafic granulites. However, in order to evaluate the effect of pressure on calculated temperature results by the garnet–clinopyroxene Fe–Mg thermometry, metamorphic temperatures for the garnet pyroxenites and the HP mafic granulites at both 10 kbar and 12 kbar have been calculated.

The temperatures measured for the garnet and clinopyroxene cores (Table S5), using the garnet–clinopyroxene Fe–Mg thermometer at 10 kbar are, 776 °C and 754 °C for the

343 garnet pyroxenites (Table 2; Figure 7), and 671 °C and 725 °C for the HP mafic
344 granulites (Table 2; Figure 7), which are ~10 °C lower than those at 12 kbar (Table 2;
345 Figure 7). However, when the compositions of garnet core and re-integrated
346 pre-exsolution original composition of clinopyroxene were applied to Fe–Mg
347 thermometer, there was a shift in the temperature, and the obtained temperatures are 818
348 °C and 800 °C at 10 kbar for the garnet pyroxenites (Table 2; Figure 7), and 698 °C and
349 767 °C at 10 kbar for the HP mafic granulites (Table 2; Figure 7). These results are also
350 ~10 °C lower than those at 12 kbar (Table 2; Figure 7). It should also be noted that the
351 temperatures using the re-integrated pre-exsolution original compositions of
352 clinopyroxene are ~30–50 °C higher than those using clinopyroxene cores under the same
353 pressure, with the same compositions of garnet core (Table 2; Figure 7).

354 **Mg isotopic compositions of clinopyroxene and garnet**

355 Mg isotopic compositions of garnet and clinopyroxene are listed in Table 3.
356 Clinopyroxenes and garnets from both the garnet pyroxenites and the HP mafic granulites
357 have obviously different δ^{26}Mg values (Table 3; Figure 8a), suggesting large
358 inter-mineral Mg isotope fractionations between clinopyroxene and garnet (Table 4;
359 Figure 8a). For the garnet pyroxenite sample 18ID-39, the δ^{26}Mg values of clinopyroxene
360 and garnet are −0.04 ± 0.04‰ and −0.65 ± 0.07‰, respectively, which are similar to
361 those of the garnet pyroxenite sample 18ID-41 (Table 3; Figure 8a). The δ^{26}Mg values of
362 clinopyroxenes from the HP mafic granulites are 0.03 ± 0.05‰ and 0.07 ± 0.03‰, which

363 are slightly higher than those of clinopyroxenes from the garnet pyroxenites (Table 3;
364 Figure 8a). The garnets from the HP mafic granulites have δ^{26}Mg values of −0.54 ± 0.11‰
365 and −0.55 ± 0.09‰, which are slightly higher than those of garnets from the garnet
366 pyroxenites (Table 3; Figure 8a). However, similar $\Delta^{26}Mg_{clinopyroxene–garnet}$ values are
367 obtained for the garnet pyroxenites (0.62‰ and 0.57‰) and the HP mafic granulites
368 (0.57‰ and 0.62‰) (Table 4).

369 **Temperature evaluation using the clinopyroxene–garnet Mg isotope thermometry**

370 The calibration of the clinopyroxene–garnet Mg isotope thermometer of Li et al. (2016)
371 yielded metamorphic temperatures of 994 ± 60 °C and 1048 ± 89 °C respectively for the
372 two samples of garnet pyroxenites, and 1048 ± 89 °C and 994 ± 65 °C for the HP mafic
373 granulites (Table 4; Figure 8b). Similar to the garnet–clinopyroxene Fe–Mg thermometry,
374 in order to evaluate the effect of pressure on the calculated temperature using the
375 clinopyroxene–garnet Mg isotope thermometer of Huang et al. (2013), metamorphic
376 temperatures for the garnet pyroxenites and the HP mafic granulites at both 10 kbar and
377 12 kbar were determined. At 10 kbar, the clinopyroxene–garnet Mg isotope thermometer
378 of Huang et al. (2013) yielded temperatures of 1038 ± 42 °C and 1093 ± 72 °C for the
379 garnet pyroxenites, and 1094 ± 71 °C and 1038 ± 47 °C for the HP mafic granulites
380 (Table 4; Figure 8b). At 12 kbar, however, the obtained temperatures are 1045 ± 43 °C
381 and 1100 ± 72 °C for the garnet pyroxenites, and 1101 ± 71 °C and 1044 ± 48 °C for the
382 HP mafic granulites (Table 4; Figure 8b).

383 # DISCUSSION

384 ## Implications of metamorphic temperatures from garnet–clinopyroxene Fe–Mg
385 ## thermometry

386 As mentioned above, the temperatures at 10 kbar from the garnet–clinopyroxene Fe–Mg
387 thermometry are ~10 °C lower than those using the same mineral compositions at 12 kbar
388 (Table 2). Thus, the effect of pressure on the temperature results is limited. Frost and
389 Chacko (1989) concluded that pre-exsolution composition of clinopyroxene was required
390 to obtain higher temperatures from the garnet–clinopyroxene Fe–Mg thermometer, and if
391 these lamellae are lost, any evidence of high temperatures will be masked. This is
392 consistent with that the temperatures using the re-integrated pre-exsolution compositions
393 of clinopyroxene are ~30–50 °C higher than those using clinopyroxene cores under the
394 same pressure, with the same compositions of garnet cores (Table 2), and should be
395 closer to peak temperature conditions.
396
397 The peak temperature conditions for the garnet pyroxenites and the HP mafic granulites
398 in this study, have been constrained from phase equilibrium modelling, which is now
399 considered generally as the most common method to constrain the peak *P–T* conditions
400 of metamorphic rocks. The peak temperature condition of the garnet pyroxenites is 1080–
401 1130 °C at 8.7–10.7 kbar (Figure 6b), whereas that of the HP mafic granulites is 1070–
402 1110 °C at 11.5–12.2 kbar (Figure 6d). When compared with the peak temperature

403 conditions calculated using the phase equilibrium modelling, metamorphic temperatures
404 from the garnet–clinopyroxene Fe–Mg thermometry, using the re-integrated
405 pre-exsolution original compositions of clinopyroxene, for the garnet pyroxenites at 10
406 kbar, are ~260–280 °C lower (Table 2), and those for the HP mafic granulites at 12 kbar
407 are ~290–360 °C lower (Table 2). Therefore, metamorphic temperatures by the garnet–
408 clinopyroxene Fe–Mg thermometry in this study are clearly inconsistent with the peak
409 temperature conditions, and only represent the retrograde metamorphic conditions. This
410 reflects that significant inter-mineral Fe–Mg exchange has occurred between garnet and
411 clinopyroxene during the retrograde cooling, which is usual for mafic granulites and
412 mantle rocks (Frost and Chacko 1989; Smith and Barron 1991; Ganguly et al. 1998;
413 Paquin and Altherr 2001; Usuki et al. 2017; Yang and Wei 2017). Also, all the garnets and
414 clinopyroxenes from the garnet pyroxenites and HP mafic granulites in this study have
415 relatively homogeneous Fe and Mg contents, with minor variation in the rim (Table S1–4;
416 Figure 5). All these results suggest re-equilibration of the garnets and clinopyroxenes
417 during the retrograde cooling, after being homogenized at granulite-facies condition.

418 **Significance of temperatures from clinopyroxene–garnet Mg isotope thermometry**

419 The metamorphic temperatures obtained using the clinopyroxene–garnet Mg isotope
420 thermometry at 10 kbar and 12 kbar are slightly different (Table 4; Figure 8b). This is
421 consistent with fact that the effect of pressure is minimal on Mg isotope fractionations
422 between garnet and clinopyroxene at equilibrium, for those rocks formed under extremely

high metamorphic temperatures (Huang et al. 2013). In addition, metamorphic temperatures estimated by the clinopyroxene–garnet Mg isotope thermometer of Huang et al. (2013) are slightly higher than those from that of Li et al. (2016) (Table 4; Figure 8b).

Metamorphic temperatures of 994 ± 60 °C and 1048 ± 89 °C for the garnet pyroxenites, and 1048 ± 89 °C and 994 ± 65 °C for the HP mafic granulites (Table 4; Figure 8b), from the clinopyroxene–garnet Mg isotope thermometer of Li et al. (2016), are similar or close to the peak temperature conditions for the corresponding samples from the phase equilibrium modelling within error (Figure 9a, b). Similarly, those metamorphic temperatures at both 10 kbar and 12 kbar (Table 4; Figure 8b), from the clinopyroxene–garnet Mg isotope thermometer of Huang et al. (2013), consistent with the peak temperature conditions for the corresponding samples from the *P–T* phase equilibrium modelling within error (Figure 9a, b). In addition, the inter-mineral Mg isotope fractionations between the garnet and clinopyroxene from the garnet pyroxenites and the HP mafic granulites are similar, and more or less fall within the equilibrium fractionation lines (Huang et al. 2013; Li et al. 2016) (Figure 9), clearly indicating equilibrium fractionation that formed during the UHT metamorphism. Therefore, metamorphic temperatures from the clinopyroxene–garnet Mg isotope thermometers (Huang et al. 2013; Li et al. 2016) are valid and can be successfully applied to constrain the peak metamorphic temperature conditions that have undergone UHT metamorphism, like the

444 pyroxenites and HP mafic granulites in this study.

445 **Effect of the retrograde cooling on equilibrium Mg isotope fractionation during the**
446 **UHT metamorphism**

447 Experimental studies have found large Mg isotope fractionation associated with diffusion
448 of Mg along chemical and temperature gradients (Richter et al. 2008; Huang et al. 2009,
449 2010; Chopra et al. 2012). Further studies on natural samples confirmed that there were
450 Mg isotope fractionations related to chemical diffusions at both mineral and outcrop
451 scales (Teng et al. 2011; Chopra et al. 2012; Sio et al. 2013; Oeser et al. 2015; Pogge Von
452 Strandmann et al. 2015; Teng 2017). At mineral scale, Teng et al. (2011) found large Mg
453 isotopic variation (up to 0.45‰ for δ^{26}Mg) in olivine fragments from Hawaiian basalts,
454 which was caused by diffusive exchange of Mg and Fe between olivines and melts during
455 cooling. Moreover, large disequilibrium inter-mineral Mg isotope fractionation, induced
456 by diffusion, during mantle metasomatism or subsolidus Mg–Fe exchange between
457 coexisting minerals, was also observed in mantle rocks (Hu et al. 2016; Xiao et al. 2016).
458
459 The clinopyroxene–garnet Mg isotope thermometer (Li et al. 2016; Huang et al. 2013),
460 yielded the peak metamorphic conditions for the garnet pyroxenites and the HP mafic
461 granulites in this study, suggesting equilibrium Mg isotope fractionations happened
462 during the UHT metamorphism. However, the retrograde metamorphic conditions
463 obtained for the garnet pyroxenites and the HP mafic granulites using the garnet–

clinopyroxene Fe–Mg thermometry, reveal significant inter-diffusion exchange of Fe and Mg occurred between garnet and clinopyroxene during the retrograde cooling. These results suggest that the inter-mineral Fe–Mg exchange occurred between garnet and clinopyroxene during the retrograde cooling of the UHT rocks didn't change their Mg isotope equilibrium obtained during the UHT metamorphic condition. Similar large HT to UHT Mg isotope fractionations between garnet and clinopyroxene have been reported in cratonic eclogites from South Africa and the Sierra Leone, West Africa (Wang et al. 2012, 2015). In this study, the published major elemental and Mg isotopic compositions were compiled for the garnet and clinopyroxene in both cratonic eclogites (Hills and Haggerty 1989; Williams et al. 2009; Wang et al. 2012, 2015) and orogenic eclogites (Li et al. 2011, 2016) (Table S6). We have recalculated their mineral formula with the same method in this study, and corresponding metamorphic temperatures using the garnet–clinopyroxene Fe–Mg thermometry (Figure 9; Table S6). The garnet–clinopyroxene Fe–Mg thermometry yielded higher metamorphic temperatures for the cratonic eclogites than those for the orogenic eclogites (Figure 9). As shown in Figure 9, the degrees of inter-mineral Mg isotope fractionations between garnet and clinopyroxene in the cratonic eclogites, are close to those of the garnet pyroxenites and HP mafic granulites in this study, but lower than those of the orogenic eclogites. In addition, unlike the garnet pyroxenites and HP mafic granulites in this study, most samples of these cratonic and orogenic eclogites have Mg isotope fractionations between garnet and clinopyroxene, falling on or near equilibrium fractionation lines (Figure 9), if the adopted metamorphic

temperatures were estimated by using the garnet–clinopyroxene Fe–Mg thermometry. These indicate limited inter-mineral diffusion of Fe–Mg between garnet and clinopyroxene in the most cratonic and orogenic eclogite samples. For the orogenic eclogites, the limited inter-mineral diffusion of Fe–Mg between garnet and clinopyroxene is due to their low peak metamorphic temperatures (Table S6). However, the different degrees of inter-mineral diffusion of Fe–Mg between garnet and clinopyroxene in the most cratonic eclogite samples, and the garnet pyroxenites and HP mafic granulites in this study, may reflect different thermal evolutions after peak temperature metamorphism.

IMPLICATIONS

This study demonstrates that the clinopyroxene–garnet Mg isotope thermometry (Li et al. 2016; Huang et al. 2013), is a valid tool to constrain the peak temperature conditions for the garnet pyroxenites and HP mafic granulites that have undergone UHT metamorphism. The Mg isotope equilibrium between garnet and clinopyroxene that formed during the UHT metamorphism is not disturbed by the inter-mineral diffusion exchange of Fe–Mg during the retrograde cooling. Our results are inconsistent with the general understanding that chemical diffusion will certainly cause the Mg isotope fractionation (Richter et al. 2008; Huang et al. 2009, 2010; Teng et al. 2011; Chopra et al. 2012; Sio et al. 2013; Oeser et al. 2015; Teng 2017). However, there still remains an ambiguity that why the Mg isotope fractionation was not disturbed by the inter-mineral diffusion exchange of Fe–Mg during the retrograde cooling. Further experiments and investigations on natural samples

505 are required to clarify this question.

506 ## ACKNOWLEDGMENTS

507 This work was jointly supported by the National Natural Science Foundation of China
508 (Grant No. 41890831) and a research grant from the State Key Laboratory of Continental
509 Dynamics (SKLCD-04). We thank Dr. K. Sajeev for his help during the field work, and
510 Dr. Zhi-An Bao for his help in analysis of Mg isotopic compositions. The authors would
511 like to thank the Govt. of India for granting the required permissions.

512

513 ## REFERENCES CITED

514 An, Y.J., Wu, F., Xiang, Y.X., Nan, X.Y., Yu, X., Yang, J.H., Yu, H.M., Xie, L.W., and
515 Huang, F. (2014) High-precision Mg isotope analyses of low-Mg rocks by
516 MC-ICP-MS. Chemical Geology, 390, 9–21.

517 Anderson, J.R., Payne, J.L., Kelsey D.E., Hand, M., Collins, A.S., and Santosh, M. (2012)
518 High-pressure granulites at the dawn of the Proterozoic. Geology, 40, 431–434.

519 Bao, Z.A., Huang, K.J., Huang, T.Z., Shen, B., Zong, C.L., Chen, K.Y., and Yuan, H.L.
520 (2019) Precise magnesium isotope analyses of high-K and low-Mg rocks by
521 MC-ICP-MS. Journal of Analytical Atomic Spectrometry, 34, 940–953.

522 Bao, Z.A., Huang, K.J., Xu, J., Deng, L., Yang, S.F., Zhang, P., and Yuan, H.L. (2020)
523 Preparation and characterization of a new reference standard GSB-Mg for Mg isotopic
524 analysis. Journal of Analytical Atomic Spectrometry, 35, 1080–1086.

525 Bizzarro, M., Paton, C., Larsen, K., Schiller, M., Trinquier, A., and Ulfbeck, D. (2011)
526 High-precision Mg-isotope measurments of terrestrial and extraterrestrial material by
527 HR-MC-ICPMS-implications for the relative and absolute Mg isotope composition of
528 the bulk silicate Earth. Journal of Analytical Atomic Spectrometry, 26, 565–577.
529 Bohlen, S.R., and Mezger, K. (1989) Origin of Granulite Terranes and the Formation of
530 the Lowermost Continental Crust. Science, 244, 326–329.
531 Chopra, R., Richter, F.M., Bruce Watson, E., and Scullard, C.R. (2012) Magnesium
532 isotope fractionation by chemical diffusion in natural settings and in laboratory
533 analogues. Geochimica et Cosmochimica Acta, 88, 1–18.
534 Chowdhury, P., and Chakraborty, S. (2019) Slow Cooling at Higher Temperatures
535 Recorded within High-P Mafic Granulites from the Southern Granulite Terrain, India:
536 Implications for the Presence and Style of Plate Tectonics near the Archean–
537 Proterozoic Boundary. Journal of Petrology, 60, 441–486.
538 Cipar, J.H., Garber, J.M., Kylander-Clark, A.R.C., and Smye, A.J. (2020) Active crustal
539 differentiation beneath the Rio Grande Rift. Nature Geoscience, 13, 758–763.
540 Fitzsimons, I.C.W., and Harley, S.L. (1994) The Influence of Retrograde Cation
541 Exchange on Granulite P–T Estimates and a Convergence Technique for the Recovery
542 of Peak Metamorphic Conditions. Journal of Petrology, 35, 543–576.
543 Frost, B.R., and Chacko, A.T. (1989) The Granulite Uncertainty Principle: Limitations on
544 Thermobarometry in Granulites. The Journal of Geology, 97, 435–450.
545 Galy, A., Yoffe, O., Janney, P. E., Williams, R. W., Cloquet, C., and Alard, O., Halicz, L.,

546 Wadhwa, M., Hutcheon, I.D., Ramon, E., and Carignan, J. (2003) Magnesium isotope
547 heterogeneity of the isotopic standard SRM980 and new reference materials for
548 magnesium-isotope-ratio measurements. Journal of Analytical Atomic Spectrometry,
549 18, 1352–1356.
550 Ganguly, J., Cheng, W., and Chakraborty, S. (1998) Cation diffusion in aluminosilicate
551 garnets: experimental determination in pyrope-almandine diffusion couples.
552 Contributions to Mineralogy and Petrology, 131, 171–180.
553 George, P.M., and Sajeev, K. (2015) Crustal evolution of Kolli-Massif, southern India:
554 Journal of Indian Institute of Science, 95, 187–201.
555 George, P.M., Sajeev, K., Santosh, M., and Zhai, M.G. (2019) Granulite-grade garnet
556 pyroxenite from the Kolli-massif, southern India: Implications for Archean crustal
557 evolution. Lithos, 342–343, 499–512.
558 Glorie, S., De Grave, J., Singh, T., Payne, J.L., and Collins, A.S. (2014) Crustal root of
559 the Eastern Dharwar Craton: Zircon U–Pb age and Lu–Hf isotopic evolution of the
560 East Salem Block, southeast India. Precambrian Research, 249, 229–246.
561 Green, E.C., White, R.W., Diener, J.F., Powell, R., Holland, T.J., and Palin, R.M. (2016)
562 Activity–composition relations for the calculation of partial melting equilibria in
563 metabasic rocks. Journal of Metamorphic Geology, 34, 845–869.
564 Harley, S.L. (1989) The origins of granulites; a metamorphic perspective. Geological
565 Magazine, 126, 215–247.
566 Harley, S.L. (1998) On the occurrence and characterization of ultrahigh-temperature

crustal metamorphism. Geological Society, London, Special Publications, 138, 81–107.

He, H.L., Wang, Y.Q., Bao, Z.A., George, P.M., Veni, S., Sajeev, K., Guo, J.H., Zhai, M.G., and Lai, K.C. (2020) Role of melt injection and mixing in the formation of chromitite in Archean megacrystic anorthosites: Evidence from the Sittampundi anorthosite complex, southern India. Precambrian Research, 350, in press.

He, H.L., Wang, Y.Q., George, P.M., Sajeev, K., Guo, J.H., Lai, C.K., and Zhai, M.G. (2021) Formation of ~2.5 Ga Sittampundi anorthosite complex in southern India: Implications to lower crustal stabilization of the Dharwar Craton, Precambrian Research, 354, in press.

Hills, D.V., and Haggerty, S.E. (1989) Petrochemistry of eclogites from the Koidu Kimberlite Complex, Sierra Leone. Contributions to mineralogy and petrology, 103, 397–422.

Holland, T.J.B., and Powell, R. (1998) An internally consistent thermodynamic data set for phases of petrological interest. Journal of Metamorphic Geology, 16, 309–343.

Holland, T.J.B., and Powell, R. (2011) An improved and extended internally consistent thermodynamic dataset for phases of petrological interest, involving a new equation of state for solids. Journal of Metamorphic Geology, 29, 333–383.

Hu, Y., Teng, F.Z., Zhang, H.F., Xiao, Y., and Su, B.X. (2016) Metasomatism-induced mantle magnesium isotopic heterogeneity: Evidence from pyroxenites. Geochimica et Cosmochimica Acta, 185, 88–111.

588 Huang, F., Lundstrom, C.C., Glessner, J., Ianno, A., Boudreau, A., Li, J., Ferré, E.C.,
589 Marshak, S., and DeFrates, J. (2009) Chemical and isotopic fractionation of wet
590 andesite in a temperature gradient: Experiments and models suggesting a new
591 mechanism of magma differentiation. Geochimica et Cosmochimica Acta, 73, 729–
592 749.
593 Huang, F., Chakraborty, P., Lundstrom, C.C., Holmden, C., Glessner, J.J.G., Kieffer,
594 S.W., and Lesher, C.E. (2010) Isotope fractionation in silicate melts by thermal
595 diffusion. Nature, 464, 396–400.
596 Huang, F., Chen, L.J., Wu, Z.Q., and Wang, W. (2013) First-principles calculations of
597 equilibrium Mg isotope fractionations between garnet, clinopyroxene, orthopyroxene,
598 and olivine: Implications for Mg isotope thermometry. Earth and Planetary Science
599 Letters, 367, 61–70.
600 Ishwar-Kumar, C., Windley, B.F., Horie, K., Kato, T., Hokada, T., Itaya, T., Yagi, K.,
601 Gouzu, C., and Sajeev, K. (2013) A Rodinian suture in western India: New insights on
602 India-Madagascar correlations. Precambrian Research, 236, 227–251.
603 Korhonen, F.J., Brown, M., Clark, C., and Bhattacharya, S. (2013) Osumilite–melt
604 interactions in ultrahigh temperature granulites: phase equilibria modelling and
605 implications for the *P–T–t* evolution of the Eastern Ghats Province, India. Journal of
606 Metamorphic Geology, 31, 881–907.
607 Li, W.Y., Teng, F.Z., Xiao, Y.L., and Huang, J. (2011) High-temperature inter-mineral
608 magnesium isotope fractionation in eclogite from the Dabie orogen, China. Earth and

609 Planetary Science Letters, 304, 224–230.

610 Li, W.Y., Teng, F.Z., Xiao, Y.L., Gu, H.O., Zha, X.P., and Huang, J. (2016) Empirical
611 calibration of the clinopyroxene–garnet magnesium isotope geothermometer and
612 implications. Contributions to Mineralogy and Petrology, 171, 61.

613 Mohan, M.R., Satyanarayanan, M., Santosh, M., Sylvester, P.J., Tubrett, M., and Lam, R.
614 (2013) Neoarchean suprasubduction zone arc magmatism in southern India:
615 Geochemistry, zircon U–Pb geochronology and Hf isotopes of the Sittampundi
616 Anorthosite Complex. Gondwana Research, 23, 539–557.

617 Oeser, M., Dohmen, R., Horn, I., Schuth, S., and Weyer, S. (2015) Processes and time
618 scales of magmatic evolution as revealed by Fe–Mg chemical and isotopic zoning in
619 natural olivines. Geochimica et Cosmochimica Acta, 154, 130–150.

620 Paquin, J., and Altherr, R. (2001) New Constraints on the P–T Evolution of the Alpe
621 Arami Garnet Peridotite Body (Central Alps, Switzerland). Journal of Petrology, 42,
622 1119–1140.

623 Pattison, D.R.M., Chacko, T., Farquhar, J., and Mcfarlane, C.R.M. (2003) Temperatures
624 of Granulite-facies Metamorphism: Constraints from Experimental Phase Equilibria
625 and Thermobarometry Corrected for Retrograde Exchange. Journal of Petrology, 44,
626 867–900.

627 Peng, P., Qin, Z.Y., Sun, F.B., Zhou, X.T., Guo, J.H., Zhai, M.G., and Ernst, R.E. (2019)
628 Nature of charnockite and Closepet granite in the Dharwar Craton: Implications for the
629 architecture of the Archean crust. Precambrian Research, 334, in press.

630 Powell, R., Holland, T.J., and Worley, B. (1998) Calculating phase diagrams involving
631 solid solutions via non-linear equations, with examples using THERMOCALC.
632 Journal of Metamorphic Geology, 16, 577–588.
633 Pogge Von Strandmann, P.A.E., Dohmen, R., Marschall, H.R., Schumacher, J.C., and
634 Elliott, T. (2015) Extreme Magnesium Isotope Fractionation at Outcrop Scale Records
635 the Mechanism and Rate at which Reaction Fronts Advance. Journal of Petrology, 56,
636 33–58.
637 Ravna, K. (2000) The garnet–clinopyroxene Fe^{2+}–Mg geothermometer: an updated
638 calibration. Journal of Metamorphic Geology, 18, 211–219.
639 Richter, F.M., Watson, E.B., Mendybaev, R.A., Teng, F.Z., and Janney, P.E. (2008)
640 Magnesium isotope fractionation in silicate melts by chemical and thermal diffusion.
641 Geochimica et Cosmochimica Acta, 72, 206–220.
642 Saitoh, Y., Tsunogae, T., Santosh, M., Chetty, T.R.K., and Horie, K. (2011). Neoarchean
643 high-pressure metamorphism from the northern margin of the Palghat–Cauvery Suture
644 Zone, southern India: Petrology and zircon SHRIMP geochronology. Journal of Asian
645 Earth Sciences, 42, 268–285.
646 Sato, K., Santosh, M., Tsunogae, T., Chetty, T.R.K., and Hirata, T. (2011) Laser ablation
647 ICP mass spectrometry for zircon U–Pb geochronology of metamorphosed granite
648 from the Salem Block: Implication for Neoarchean crustal evolution in southern India.
649 Journal of Mineralogical and Petrological Sciences, 106, 1–12.
650 Sawyer, E.W., Cesare, B., and Brown, M. (2011) When the Continental Crust Melts.

651 Elements, 7, 229–234.

652 Sio, C.K.I., Dauphas, N., Teng, F.Z., Chaussidon, M., Helz, R.T., and Roskosz, M. (2013)
653 Discerning crystal growth from diffusion profiles in zoned olivine by in situ Mg–Fe
654 isotopic analyses. Geochimica et Cosmochimica Acta, 123, 302–321.

655 Smith, D., and Barron, B.R. (1991) Pyroxene-garnet equilibration during cooling in the
656 mantle. American Mineralogist, 76, 1950–1963.

657 Talukdar, M., Mukhopadhyay, D., Sanyal, S., and Sengupta, P. (2020) Early
658 Palaeoproterozoic structural reconstitution of a suite of rocks from the Mahadevi
659 Layered Complex, Tamil Nadu, India. Geological Journal, 55, 3615–3642.

660 Teng, F.Z., Li, W.Y., Ke, S., Yang, W., Liu, S.A., Sedaghatpour, F., Wang, S.J., Huang,
661 K.J., Hu, Y., Ling, M.X., Xiao, Y., Liu, X.M., Li, X.W., Gu, H.O., Sio, C.K., Wallace,
662 D.A., Su, B.X., Zhao, L., Chamberlin, J., Harrington, M., and Brewer, A. (2015)
663 Magnesium isotopic compositions of international geological reference materials.
664 Geostandards and Geoanalytical Research, 39, 329–339.

665 Teng, F.Z. (2017) Magnesium Isotope Geochemistry. Reviews in Mineralogy and
666 Geochemistry, 82, 219–287.

667 Teng, F.Z., Dauphas, N., Helz, R.T., Gao, S., and Huang, S.C. (2011) Diffusion-driven
668 magnesium and iron isotope fractionation in Hawaiian olivine. Earth and Planetary
669 Science Letters, 308, 317–324.

670 Usuki, T., Iizuka, Y., Hirajima, T., Svojtka, M., Lee, H., and Jahn, B. (2017) Significance
671 of Zr-in-Rutile Thermometry for Deducing the Decompression P–T Path of a Garnet–

672 Clinopyroxene Granulite in the Moldanubian Zone of the Bohemian Massif. Journal of
673 Petrology, 58, 1173–1198.
674 Wang, S.J., Teng, F.Z., Williams, H.M., and Li, S.G. (2012) Magnesium isotopic
675 variations in cratonic eclogites: Origins and implications. Earth and Planetary Science
676 Letters, 359–360, 219–226.
677 Wang, S.J., Teng, F.Z., and Li, S.G. (2014a) Tracing carbonate-silicate interaction during
678 subduction using magnesium and oxygen isotopes. Nature Communication 5, 5328.
679 Wang, S.J., Teng, F.Z., Li, S.G., and Hong, J.A. (2014b) Magnesium isotope systematics
680 of mafic rocks during continental subduction. Geochim Cosmochim Acta 143, 34–48.
681 Wang, S.J., Teng, F.Z., Rudnick, R.L., and Li, S.G. (2015) Magnesium isotope evidence
682 for a recycled origin of cratonic eclogites. Geology 43, 1071–1074.
683 White, R.W., Powell, R., Holland, T.J.B., Johnson, T.E., and Green, E.C.R. (2014) New
684 mineral activity–composition relations for thermodynamic calculations in metapelitic
685 systems. Journal of Metamorphic Geology, 32, 261–286.
686 Whitney, D.L., and Evans, B.W. (2010) Abbreviations for names of rock-forming
687 minerals. American Mineralogist, 95, 185–187.
688 Williams, H.M., Nielsen, S.G., Renac, C., Griffin, W.L., O'Reilly, S.Y., McCammon,
689 C.A., Pearson, N., Viljoen, F., Alt, J.C., and Halliday, A.N. (2009) Fractionation of
690 oxygen and iron isotopes by partial melting processes: Implications for the
691 interpretation of stable isotope signatures in mafic rocks. Earth and Planetary Science
692 Letters, 283, 156–166.

693 Xiao, Y., Teng, F.Z., Su, B.X., Hu, Y., Zhou, M.F., Zhu, B., Shi, R.D., Huang, Q.S.,
694 Gong, X.H., and He, Y.S. (2016) Iron and magnesium isotopic constraints on the
695 origin of chemical heterogeneity in podiform chromitite from the Luobusa ophiolite,
696 Tibet. Geochemistry, Geophysics, Geosystems, 17, 940–953.
697 Yang, C., and Wei, C.J. (2017) Ultrahigh temperature (UHT) mafic granulites in the East
698 Hebei, North China Craton: Constraints from a comparison between temperatures
699 derived from REE-based thermometers and major element-based thermometers.
700 Gondwana Research, 46, 156–169.
701 Young, E.D., Manning, C.E., Schauble, E.A., Shahar, A., Macris, C.A., Lazar, C., and
702 Jordan, M. (2015) High-temperature equilibrium isotope fractionation of
703 non-traditional stable isotopes: experiments theory, and applications. Chemical
704 Geology, 395, 176–195.
705

706 **Figure captions**

707 **Figure 1.** (**a**) The location of major Archean cratons in India. (**b**) Geological map of the
708 Dharwar Craton. Abbreviations: DC, Dharwar Craton; BC, Bastar Craton; BKC,
709 Bundhelkland Craton; AC, Aravalli Craton; SC, Singbhum Craton; WDC, the Western
710 Dharwar Craton; CDC, the Central Dharwar Craton; EDC, the Eastern Dharwar Craton;
711 KSZ, Kumta shear zone; ChSZ, Chitradurga Shear Zone; CoSZ, Coorg shear zone; MSZ,
712 Moyar Shear Zone; BSZ, Bhavani Shear Zone; MKSZ: Mettur-Kolar shear zone; NSZ:

713 Nallamalai shear zone; PCSZ, Palghat-Cauvery Shear Zone; SASZ, Salem-Attur Shear
714 Zone; CSZ, Cauvery Shear Zone; ASZ, Achankovil shear zone; KKPTSZ, Karur
715 Kambam Painavu Trichur shear zone; EGMB, Eastern Ghats Mobile Belts. Figure 1b is
716 modified after Ishwar-Kumar et al. (2013), George and Sajeev(2015), George et al.
717 (2019), and He et al. (2020).

718

719 **Figure 2.** Geological map of the Namakkal Block in the southern granulite terrain, India
720 (modified after George and Sajeev (2015) and George et al. (2019)).

721

722 **Figure 3.** Photomicrographs (plane-polarized light) of the garnet pyroxenites and the HP
723 mafic granulites. (**a**) Garnet and clinopyroxene porphyroblasts in the garnet pyroxenite
724 sample 18ID-39. (**b**) Garnet and clinopyroxene porphyroblasts in the garnet pyroxenite
725 sample 18ID-41. (**c**) Garnet, clinopyroxene, orthopyroxene, plagioclase and minor
726 hornblende in the mafic granulite sample 18ID-46. (**d**) Hornblende corona around
727 orthopyroxene in the mafic granulite sample 18ID-46. (**e**) Garnet, clinopyroxene, and
728 plagioclase in the mafic granulite sample 18ID-50. (**f**) minor hornblende around
729 orthopyroxene in the mafic granulite sample 18ID-50. The yellow lines with arrow
730 denote the locations of compositional profiles. In this study, all the mineral abbreviations
731 follow Whitney and Evans (2010).

732

733 **Figure 4.** Back-scattered electron photomicrographs showing narrow orthopyroxene

734 exsolution lamellae within clinopyroxene porphyroblasts from the garnet pyroxenites and
735 the HP mafic granulites. (**a**) Garnet pyroxenite sample 18ID-39. (**b**) Garnet pyroxenite
736 sample 18ID-41. (**c**) Mafic granulite sample 18ID-46. (**d**) Mafic granulite sample
737 18ID-50.

738

739 **Figure 5.** Compositional profiles of garnet and clinopyroxene porphyroblasts from the
740 garnet pyroxenite samples 18ID-39 (**a**) and 18ID-41 (**b**), and the HP mafic granulite
741 samples 18ID-46 (**c**) and 18ID-50 (**d**).

742

743 **Figure 6.** T–X_{H2O} and P–T pseudosections for the garnet pyroxenite samples 18ID-39 and
744 the HP mafic granulite sample 18ID-50. (**a**) T–X_{H2O} pseudosection for the garnet
745 pyroxenite sample 18ID-39 at 10 kbar, with the final mineral assemblage marked by Liq–
746 grt–hbl–cpx–pl–ilm–qz in red type. (**b**) P–T pseudosection for the garnet pyroxenite
747 samples 18ID-39, with peak mineral assemblage marked by Liq–grt–cpx–pl–ilm in red
748 type. (**c**) T–X_{H2O} pseudosection for the HP mafic granulite sample 18ID-50 at 10 kbar,
749 with the final mineral assemblage marked by Liq–grt–hbl–cpx–opx–pl–ilm–qz in red
750 type. (**d**) P–T pseudosection for the HP mafic granulite sample 18ID-50, with peak
751 mineral assemblage marked by Liq–grt–cpx–opx–pl–ilm in red type, and isopleths of X_{grs}
752 in garnet, and X_{an} in plagioclase. The peak metamorphic condition of the HP mafic
753 granulite sample 18ID-50 is indicated by the field in yellow color. Red bars in (**a**) and (**c**)
754 denote H_2O contents used for subsequent modelling.

Figure 7. Plot of LnK_D versus X_{Mg}(Grt) with temperature isopleths at both 10 kbar and 14 kbar, where $K_D = (Fe^{2+}/Mg)^{Grt}/(Fe^{2+}/Mg)^{Cpx}$ and $X_{Mg}(Grt) = Mg/(Mg + Fe^{2+})$ in garnet. The LnK_D and X_{Mg}(Grt) are calculated using compositions of garnets and clinopyroxenes as same as those for the garnet–clinopyroxene Fe–Mg thermometry.

Figure 8. (**a**) δ^{26}Mg values of clinopyroxenes and garnets in the garnet pyroxenites and the HP mafic granulites. (**b**) Metamorphic temperatures calculated by the calibration of the clinopyroxene–garnet Mg isotope thermometers of Huang et al. (2013) and Li et al. (2016). Huang2013 and Li2016 mean Huang et al. (2013) and Li et al. (2016), respectively. The error bars in (**a**) and (**b**) represent the precision (2SD) on δ^{26}Mg, and the uncertainty of the estimated temperature (ΔT), respectively.

Figure 9. Plots of $\Delta^{26}Mg_{Cpx–Grt}$ versus $10^6/(T)^2$ with equilibrium Mg isotope fractionation lines from Huang et al. (2013) and Li et al. (2016). The equilibrium Mg isotope fractionation line from Huang et al. (2013) in (**a**) is at 10 kbar, and that in (**b**) is at 12 kbar. T denotes temperatures estimated by the garnet–clinopyroxene Fe–Mg thermometry, using the compositions of garnet and clinopyroxene cores, whereas T1 denotes those estimated by the garnet–clinopyroxene Fe–Mg thermometry, using the composition of garnet core and the re-integrated pre-exsolution original composition of clinopyroxene. T Pseud. means temperatures from *P–T* pseudosection modellings. The δ^{26}Mg values of

776 garnet and clinopyroxene in the cratonic eclogites are from Wang et al (2012, 2015), and
777 those in the orogenic eclogites are from Li et al (2011, 2016). Error bars represent the
778 standard deviation of the $\Delta^{26}Mg_{Cpx-Grt}$ value.

779

780 **Supplementary Figure**

781 **Figure S1.** TIMA images of the garnet pyroxenite samples 18ID-39 (**a**) and 18ID-41 (**b**),
782 and the HP mafic granulite samples 18ID-46 (**c**) and 18ID-50 (**d**).

783

784 **Tables**

785 **Table 1.** Bulk composition of the garnet pyroxenite and HP mafic granulite used for
786 phase equilibrium modelling.

787

788 **Table 2.** Metamorphic temperatures of the garnet pyroxenites and the HP mafic
789 granulites estimated by the garnet–clinopyroxene Fe–Mg thermometry.

790

791 **Table 3.** Magnesium isotopic compositions of clinopyroxenes and garnets in the garnet
792 pyroxenites and the mafic granulites, and standards.

793

794 **Table 4.** Metamorphic temperatures of the garnet pyroxenites and the mafic granulites
795 calculated by using the clinopyroxene–garnet Mg isotope geothermometer.

796

797 **Supplementary tables**

798 **Table S1.** Major element compositions of garnet, clinopyroxene, and orthopyroxene
799 lamellae in the garnet pyroxenite sample 18ID-39.

800

801 **Table S2.** Major element compositions of garnet, clinopyroxene, and orthopyroxene
802 lamellae in the garnet pyroxenite sample 18ID-41.

803

804 **Table S3.** Major element compositions of garnet, clinopyroxene, and orthopyroxene
805 lamellae in the HP mafic granulite sample 18ID-46.

806

807 **Table S4.** Major element compositions of garnet, clinopyroxene, orthopyroxene lamellae
808 and plagioclase in the HP mafic granulite sample 18ID-50.

809

810 **Table S5.** Mineral compositions used in temperatures calculated by the garnet–
811 clinopyroxene Fe–Mg thermometry.

812

813 **Table S6.** Summary of published major elemental and Mg isotopic compositions for the
814 garnet and clinopyroxene in both the cratonic and orogenic eclogites, and metamorphic
815 temperatures calculated by the garnet–clinopyroxene Fe–Mg thermometry.

Table 1

Bulk composition of the garnet pyroxenite and HP mafic granulite used for phase equilibrium modelling.

Whole rock compositions (wt.%)												
Sample	SiO_2	TiO_2	Al_2O_3	TFe_2O_3	FeO	MnO	MgO	CaO	Na_2O	K_2O	P_2O_5	LOI	Total
18ID-39	42.12	2.51	12.03	5.89	13.55	0.24	7.81	12.65	1.6	0.03	0.04	−0.36	98.11
18ID-50	51.21	0.87	15.38	2.70	7.66	0.15	6.20	11.50	3.22	0.21	0.10	−0.30	98.90

Normalized molar proportion used for phase equilibrium modelling												
Figures			H_2O	SiO_2	Al_2O_3	CaO	MgO	FeO	K_2O	Na_2O	TiO_2	O*
18ID-39	6a	x=0	0.000	43.947	7.396	14.140	12.148	16.447	0.020	1.618	1.970	2.313
		x=1	5.000	41.750	7.026	13.433	11.541	15.625	0.019	1.537	1.871	2.197
	6b		2.250	42.959	7.230	13.822	11.875	16.077	0.020	1.582	1.925	2.261
18ID-50	6c	x=0	0.000	53.795	9.520	12.942	9.710	8.860	0.141	3.279	0.687	1.066
		x=1	5.000	51.105	9.044	12.295	9.224	8.417	0.134	3.115	0.653	1.013
	6d		0.300	53.633	9.492	12.903	9.681	8.834	0.140	3.269	0.685	1.063

Table 2

Metamorphic temperatures of the garnet pyroxenites and the HP mafic granulites estimated by the garnet–clinopyroxene Fe–Mg thermometry.

Rock type	Sample number	Grt core and cpx core, at 10 kbar	Grt core and integrated cpx, at 10 kbar	Grt core and cpx core, at 12 kbar	Grt core and integrated cpx, at 12 kbar
		T (°C, R20)	*T* (°C, R20)	*T* (°C, R20)	*T* (°C, R20)
Garnet pyroxenites	18ID-39	776	818	789	832
	18ID-41	754	800	767	813
Mafic granulites	18ID-46	671	698	682	709
	18ID-50	725	767	737	780

Notes: R20 denotes Ravna (2000).

Table 3

Magnesium isotopic compositions of clinopyroxenes and garnets in the garnet pyroxenites and the mafic granulites, and standards.

Samples No.	$\delta^{26}Mg_{Cpx}$ (‰)	2SD	$\delta^{25}Mg_{Cpx}$ (‰)	2SD	$\delta^{26}Mg_{Grt}$ (‰)	2SD	$\delta^{25}Mg_{Grt}$ (‰)	2SD
Garnet pyroxenites								
18ID-39	−0.04	0.04	−0.01	0.04	−0.65	0.07	−0.36	0.03
18ID-41	−0.07	0.09	−0.05	0.05	−0.64	0.07	−0.34	0.05
Mafic granulites								
18ID-46	0.03	0.05	0.01	0.06	−0.54	0.11	−0.31	0.07
18ID-50	0.07	0.03	0.03	0.02	−0.55	0.09	−0.29	0.06
Standards	$\delta^{26}Mg$ (‰)	2SD	$\delta^{25}Mg$ (‰)	2SD				
BCR-2	−0.17	0.05	−0.11	0.03				
BHVO-2	−0.19	0.05	−0.10	0.05				
BHVO-2R	−0.17	0.04	−0.10	0.01				

Notes: (1) 2SD means two times the standard deviation of the population of n repeat measurements during an analytical session. (2) R means repeat column chemistry and measurement.

This is the peer-reviewed, final accepted version for American Mineralogist, published by the Mineralogical Society of America.
The published version is subject to change. Cite as Authors (Year) Title. American Mineralogist, in press.
DOI: https://doi.org/10.2138/am-2022-8058. http://www.minsocam.org/

Table 4

Metamorphic temperatures of the garnet pyroxenites and the mafic granulites calculated by using the clinopyroxene–garnet Mg isotope geothermometer.

Samples number	$\Delta^{26}Mg_{cpx-grt}$ (‰)	T (°C)[a]	ΔT (°C)	T (°C)[b]	ΔT (°C)	T (°C)[c]	ΔT (°C)
Garnet pyroxenites							
18ID-39	0.62	994	60	1038	42	1045	43
18ID-41	0.57	1048	89	1093	72	1100	72
Mafic granulites							
18ID-46	0.57	1048	89	1094	71	1101	71
18ID-50	0.62	994	65	1038	47	1044	48

Notes: (1) $\Delta^{26}Mg_{cpx-grt}$ (‰) = $\delta^{26}Mg_{cpx} - \delta^{26}Mg_{grt}$. (2) a denotes temperatures calculated by the Mg isotope geothermometer of Li et al. (2016), i.e., $\Delta^{26}Mg_{cpx-grt} = (0.99 \pm 0.06)\times10^6/T^2$. b and c denote temperatures calculated by the Mg isotope geothermometer of Huang et al. (2013) at P = 10 kbar and 12 kbar, respectively, i.e., $\Delta^{26}Mg_{cpx-grt} = 1.06\times10^6/T^2$ (10 kbar) and $\Delta^{26}Mg_{cpx-grt} = 1.07\times10^6/T^2$ (12 kbar). T is temperature in Kelvin. (3) ΔT is uncertainty of the estimated temperature, and is calculated follow Li et al. (2016) with formula of $\Delta T = S\Delta^{26}Mg_{cpx-grt}/(2A\times10^6/T^3) + T\times S_A/2A$, where T is also temperature in Kelvin. $S\Delta^{26}Mg_{cpx-grt}$ is the standard deviation of the $\Delta^{26}Mg_{cpx-grt}$ value, which is calculated by $(S\Delta^{26}Mg_{cpx-grt})^2 = (S\delta^{26}Mg_{cpx})^2 + (S\delta^{26}Mg_{grt})^2$, where $S\delta^{26}Mg_{cpx}$ and $S\delta^{26}Mg_{grt}$ are the standard deviation on $\delta^{26}Mg$ of clinopyroxene and garnet, respectively. A and S_A are the slope of the calibrated line and its standard deviation, respectively.

This is the peer-reviewed, final accepted version for American Mineralogist, published by the Mineralogical Society of America.
The published version is subject to change. Cite as Authors (Year) Title. American Mineralogist, in press.
DOI: https://doi.org/10.2138/am-2022-8058. http://www.minsocam.org/

Figure 1

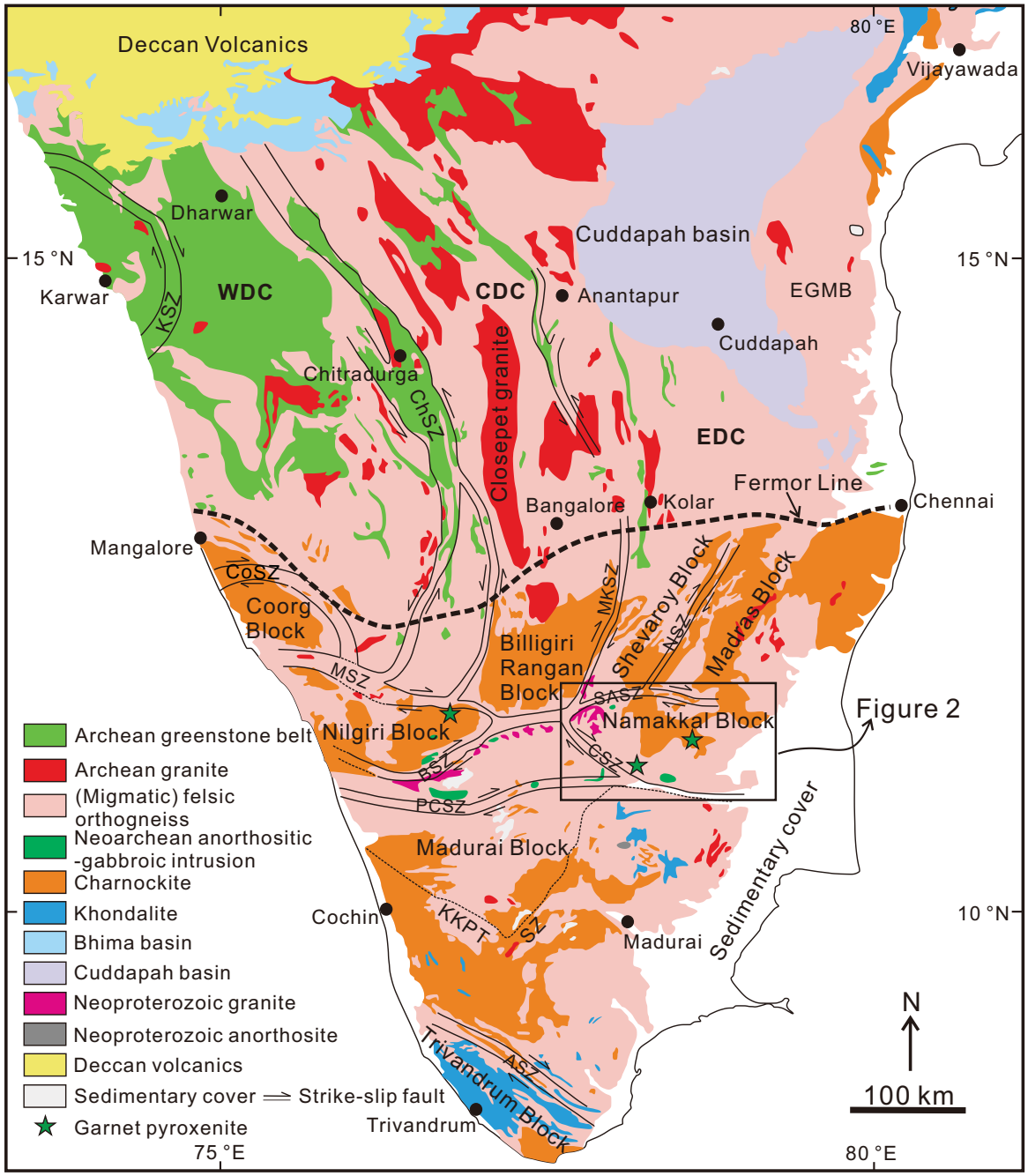

This is the peer-reviewed, final accepted version for American Mineralogist, published by the Mineralogical Society of America.
The published version is subject to change. Cite as Authors (Year) Title. American Mineralogist, in press.
DOI: https://doi.org/10.2138/am-2022-8058. http://www.minsocam.org/

Figure 2

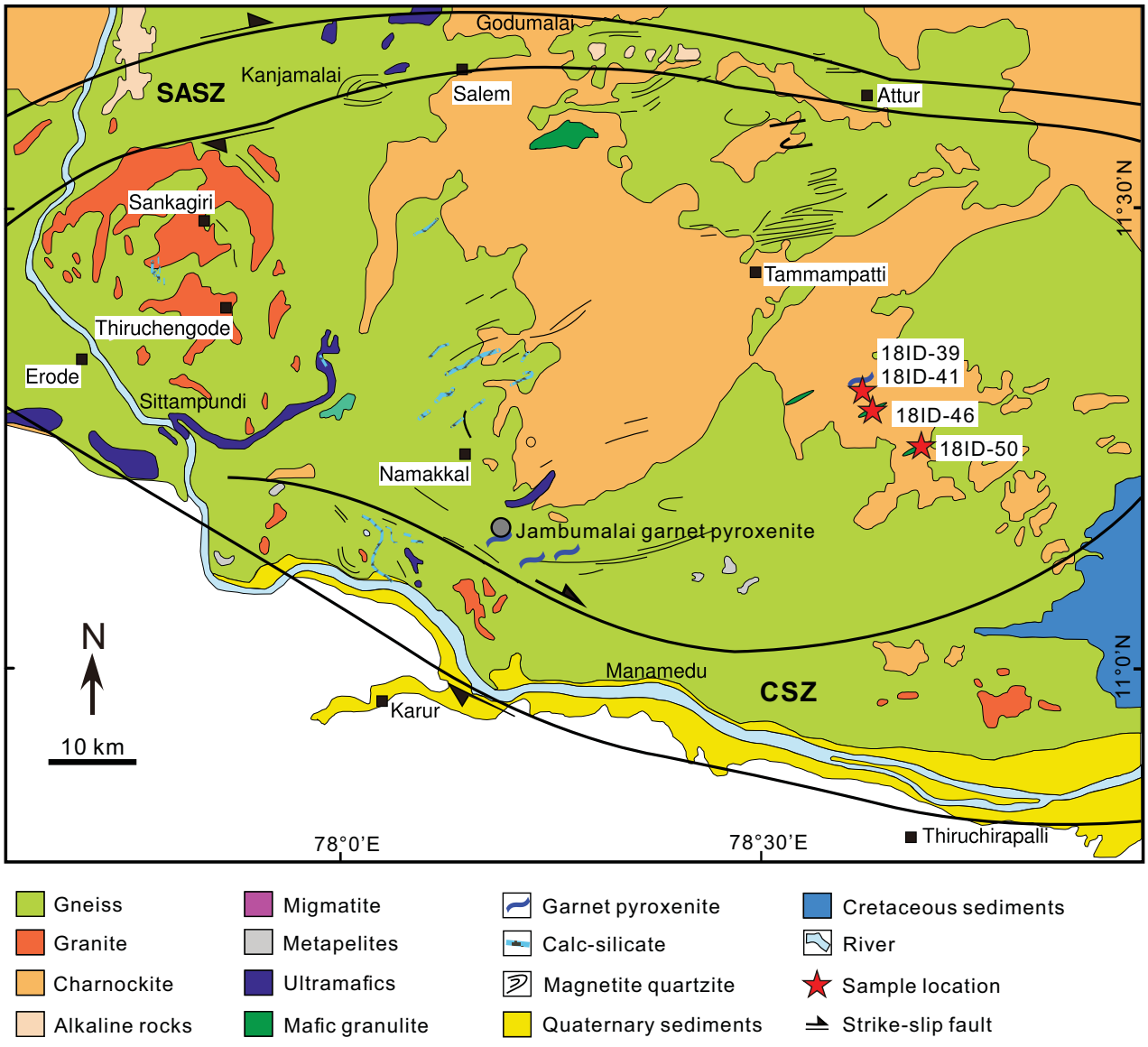

This is the peer-reviewed, final accepted version for American Mineralogist, published by the Mineralogical Society of America.
The published version is subject to change. Cite as Authors (Year) Title. American Mineralogist, in press.
DOI: https://doi.org/10.2138/am-2022-8058. http://www.minsocam.org/

Figure 3

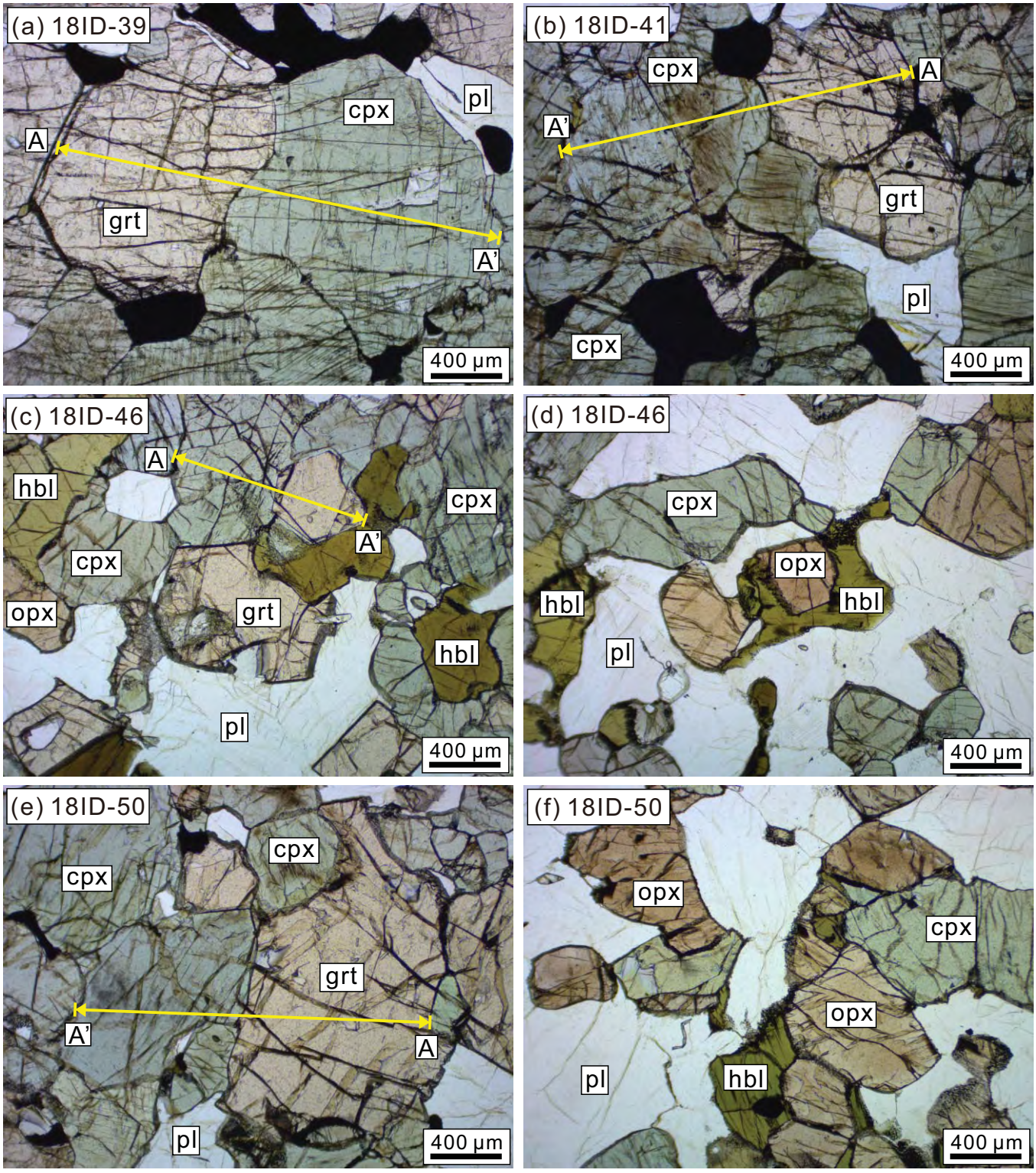

This is the peer-reviewed, final accepted version for American Mineralogist, published by the Mineralogical Society of America.
The published version is subject to change. Cite as Authors (Year) Title. American Mineralogist, in press.
DOI: https://doi.org/10.2138/am-2022-8058. http://www.minsocam.org/

Figure 4

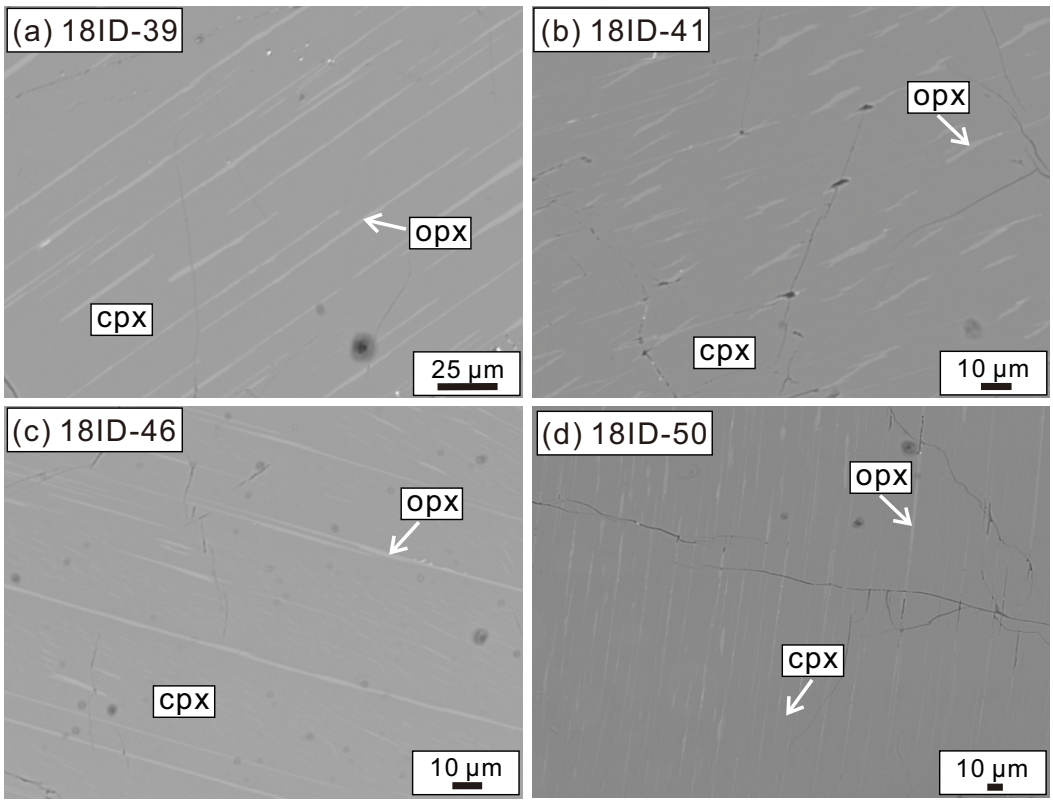

This is the peer-reviewed, final accepted version for American Mineralogist, published by the Mineralogical Society of America.
The published version is subject to change. Cite as Authors (Year) Title. American Mineralogist, in press.
DOI: https://doi.org/10.2138/am-2022-8058. http://www.minsocam.org/

Figure 5

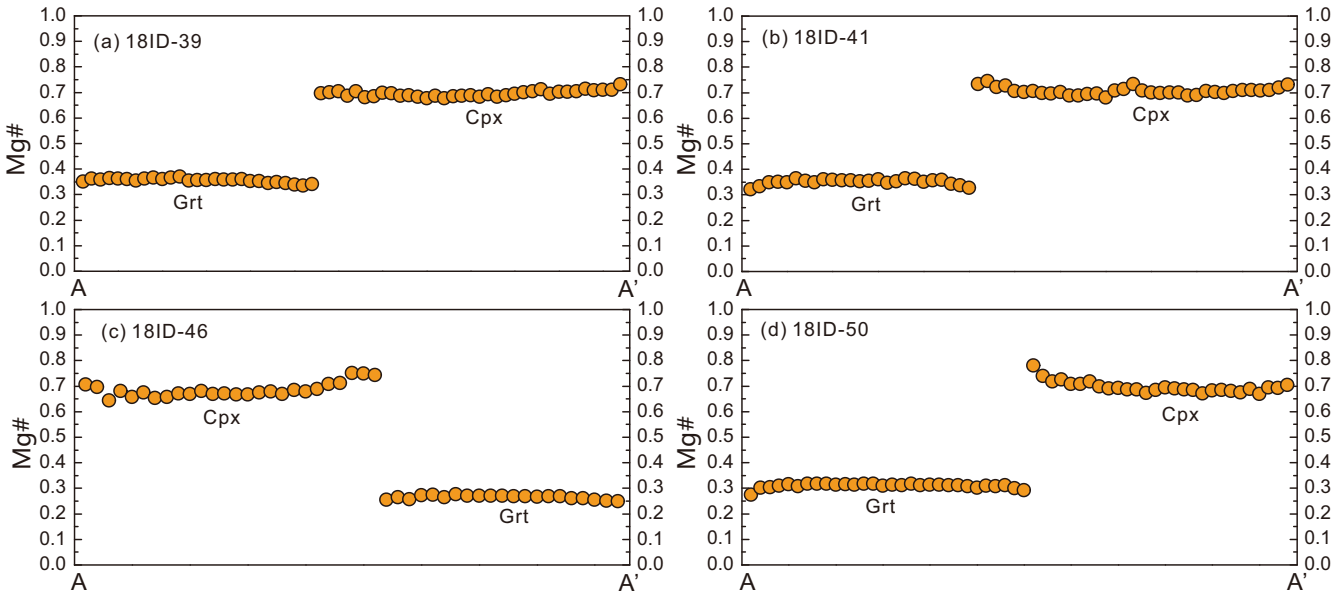

This is the peer-reviewed, final accepted version for American Mineralogist, published by the Mineralogical Society of America.
The published version is subject to change. Cite as Authors (Year) Title. American Mineralogist, in press.
DOI: https://doi.org/10.2138/am-2022-8058. http://www.minsocam.org/

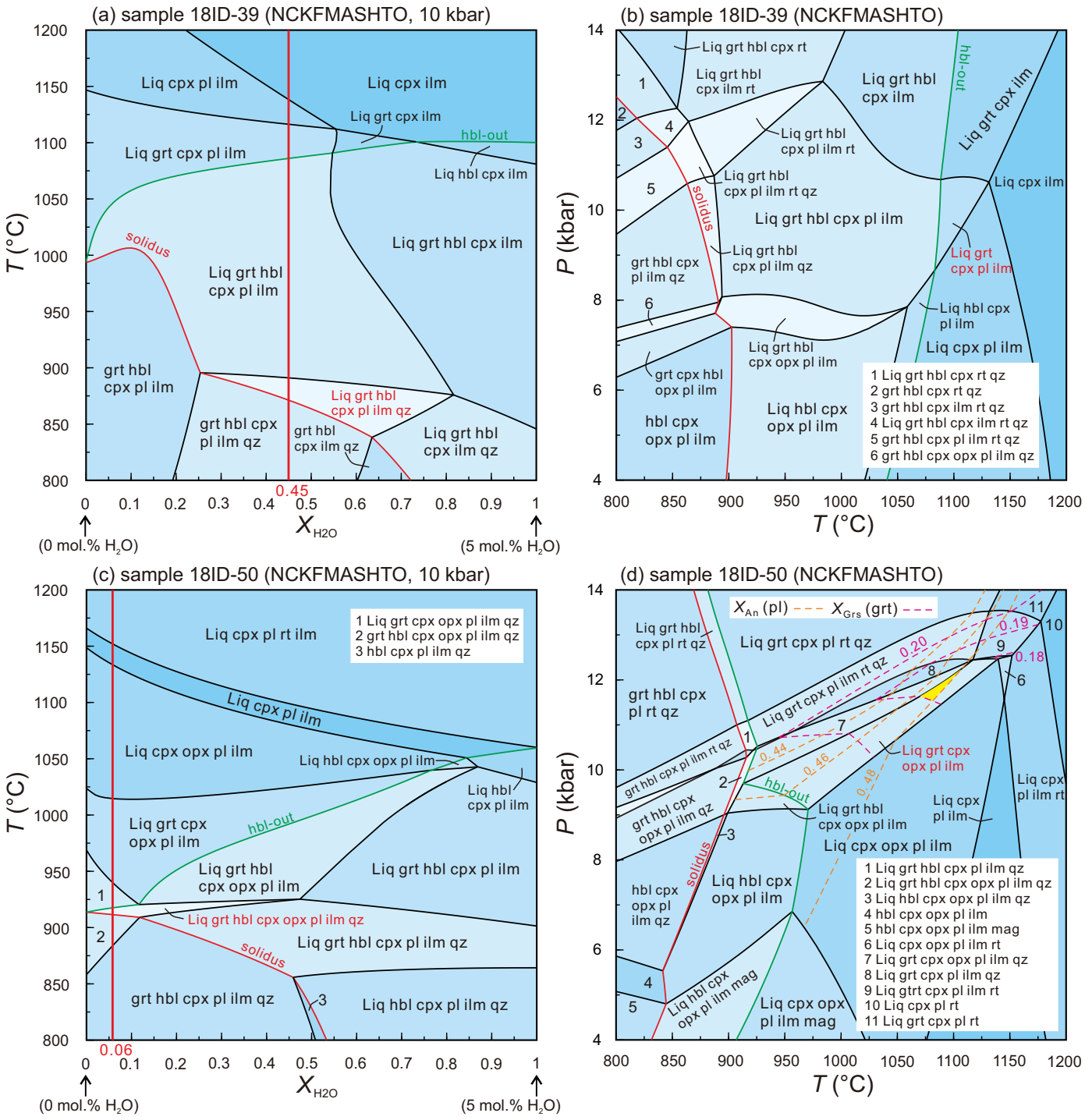

Figure 7

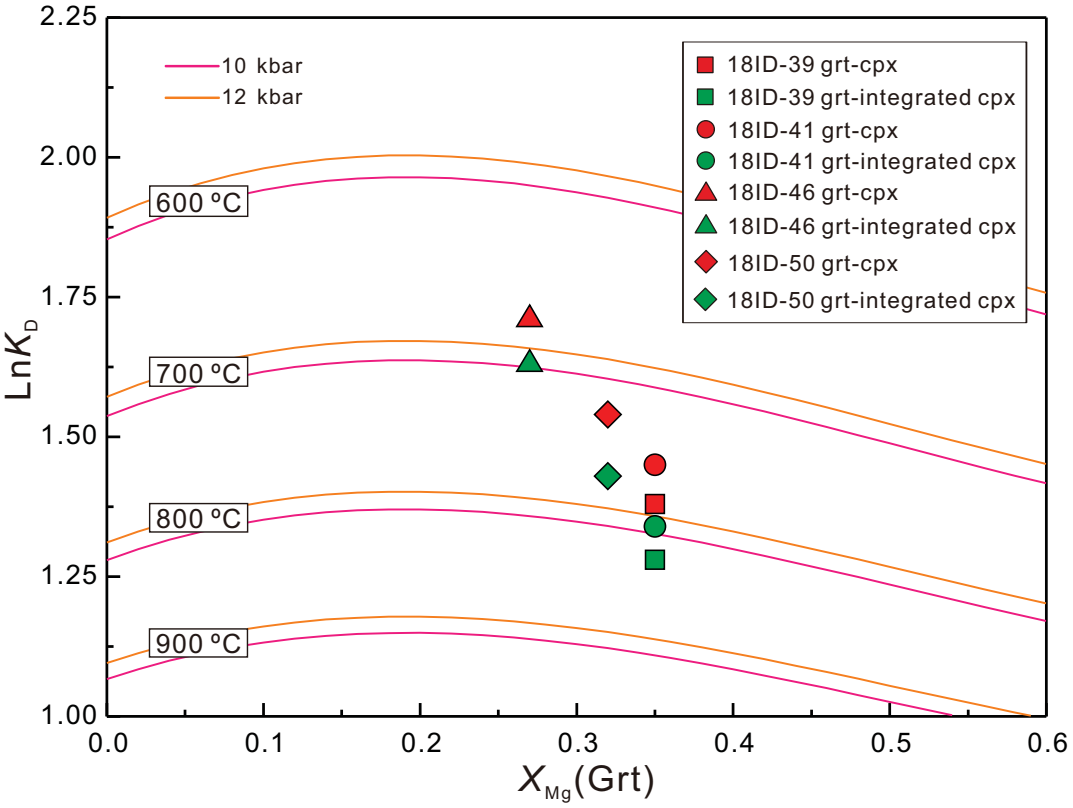

Figure 8

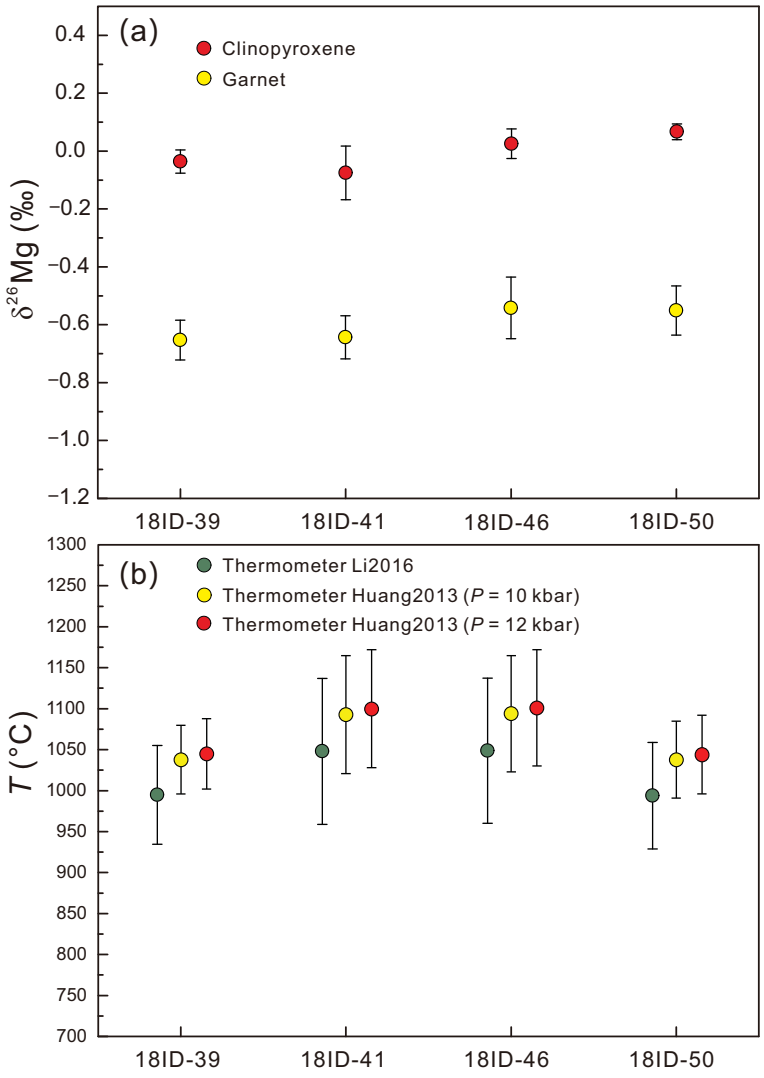

Figure 9